IEEE Access
Multidisciplinary ⋮ Rapid Review ⋮ Open Access Journal

Received April 16, 2022, accepted April 25, 2022, date of publication April 28, 2022, date of current version May 4, 2022.

Digital Object Identifier 10.1109/ACCESS.2022.3170841

Polarization Combining and Equalization in 5G Mobile-to-Mobile Systems

FARAH ARABIAN, (Graduate Student Member, IEEE), AND MICHAEL RICE, (Fellow, IEEE)
Department of Electrical and Computer Engineering, Brigham Young University, Provo, UT 84602, USA
Corresponding author: Farah Arabian (farah.arabian@byu.edu)

ABSTRACT This article develops maximum likelihood (ML) detection for post-FFT processing of dual-polarized antenna outputs with a cyclic-prefix OFDM (CP-OFDM) waveform for a frequency selective multipath fading in a 5G mobile-to-mobile setting. The suggested maximum likelihood detector (MLD) comprises a combiner applied to the channel matched filter outputs (designated MLC) followed by a decision rule based on correlation and signal energy. When MLC is coupled with a frequency-domain equalizer, this structure is called MLC+FDE. The designed MLD and MLC+FDE are compared to the traditional combining techniques: maximum ratio combining, equal gain combining, and selection combining. Computer simulations performed over a stochastic channel model with polarization state information. The simulation results show that the difference between MLD and maximum ratio combining (the best performing method), MLC+FDE (almost the best performing method) and selection diversity with frequency-domain equalization (the worst performing method) is 2 dB. This diversity improvement is limited by the correlation between the two channels that characterize the two polarization states. This correlation makes it difficult to achieve reliable transmission through combining alone; some form of error control coding is also needed. When channel estimates are used in place of perfect channel knowledge, an error floor is observed.

INDEX TERMS Frequency selective multipath fading, CP-OFDM, polarization diversity, diversity combining, equalization, 5G-FR1.

I. INTRODUCTION AND BACKGROUND

Increasing mobile data traffic in cellular networks requires an improvement in mobile-to-mobile throughput in wideband channels with frequency selective multipath fading. One way to achieve the improvement is with the application of diversity and equalization techniques.

Diversity techniques such as spatial, frequency, time, or code diversity are well known. Somewhat less known is polarization diversity. Polarization diversity, usually in the form of two outputs from co-located cross-polarized antenna elements, is an attractive technique for mobile-to-mobile communications due the compact space required to achieve it [1], [2]. The performance of polarization diversity depends on how uncorrelated the outputs of the two antenna elements are. The mobile radio channel tends to decorrelate the outputs of cross polarized antenna elements, but not completely [3], [4].

The associate editor coordinating the review of this manuscript and approving it for publication was Adao Silva.

The simplest form of diversity reception combines multiple copies of the transmitted signal. The open literature contains a large number of articles that discusses and analyzes combining the outputs of multiple antenna elements. A sampling of these articles includes [5] where the relationship between traditional diversity combining techniques such as maximum ratio combining (MRC), equal gain combining (EGC), and selection combining (SC) were developed for single-carrier and multi-carrier modulations. Mathematical expressions for the bit error probability for simple single-carrier modulations in Rayleigh fading were shown to apply to the combined outputs after the FFT operation in an OFDM detector. Reference [6] introduced a pre-FFT combining technique involving two or more consecutive OFDM symbols to reduce the number of required FFT operations. The pre-FFT combining resulted in a 3 dB performance loss compared to the post-FFT combining. These results align with two later studies [7], [8]. In [7], pre- and post-FFT combining were compared in rural and urban areas. The authors conclude that pre-FFT combining is preferred in rural areas (characterized by relatively good channels) because the pre-FFT combining only

This work is licensed under a Creative Commons Attribution 4.0 License. For more information, see https://creativecommons.org/licenses/by/4.0/

requires one FFT operation in the detector. In contrast, post-FFT combining is preferred in urban areas (characterized by rich multipath propagation); the performance advantage of post-FFT combining overcomes the complexity disadvantage. The results published in [8] compared outage capacities for pre- and post-FFT combining in both indoor and outdoor environments. Pre-FFT combining was recommended in indoor environments with low delay spreads but post-FFT combining was recommended in outdoor environments.

Post-FFT combining was examined in [9] where the best performing system applied a separate post-FFT frequency domain equalizer to each antenna branch and combined the equalizer outputs using MRC. Reference [10] also focused on post-FFT combining using MRC. Here, the goal was optimum demodulation/decoding for *independent* channels on the antenna branches. The optimum process creates soft bit metrics, combines the soft information, then decodes. In [11], pre-FFT combining and post-FFT combining were evaluated. The pre-FFT combining took the form of a beam former and MRC was applied to the bank of parallel FFT outputs.

To the best of the author's knowledge, none of the prior works on pre- or post-FFT combining in multicarrier systems considered polarization diversity (where the channels are not independent) or examined techniques beyond the traditional diversity combining techniques. Some initial results were published by the authors in [12] where it was shown that combine-then-equalize outperforms equalize-then-combine; post-FFT combining is better able to leverage the inherent diversity gain in correlated cross-polarized channels than equalizers.

This article focuses on a mobile-to-mobile link inside a cell [13]. Mobile-to-mobile communication is based on a resource pool idea in which a set of time/frequency resources (called a resource pool) is configured for mobile-to-mobile use. There are separate resources for mobile-to-mobile control and mobile-to-mobile data transmission. The mobile-to-mobile resource pool can be configured inside a single cell. The information about the resource pool is sent out via broadcast messages [14]. The resource allocation and scheduling design is not a concern in this article, however the radio channel is developed assuming a mobile-to-mobile scenario.

The first contribution of this article is the development of maximum likelihood (ML) detection for post-FFT processing of the dual-polarized antenna outputs with a cyclic-prefix OFDM (CP-OFDM) waveform in a frequency selective multipath fading environment. The optimum combining approach in the ML sense was developed by Scott [15] for single carrier modulations in the context of 2G cellular systems. Scott's ideas are extended here to the CP-OFDM case. We show that ML detection takes the form of a combiner followed by a symbol decision rule that incorporates channel state information. Motivated by the equivalent channel defined by the ML detector, we formulate a detector based on the combining defined by ML detection, followed by a frequency domain equalizer (FDE). This system is called ML combining and frequency domain equalization (MLC+FDE).

The second contribution of this article is the comparison of ML and MLC+FDE with traditional combining techniques (MRC, EGC, and SC) applied post FFT. The basis for comparison is the uncoded bit error rate (BER). We use the post-equalizer BER when an FDE is used. A three-dimensional stochastic channel model with polarization state described in [16]–[18] operating in the 5G lower frequency band (FR1) is used to generate an ensemble of vertically and horizontally polarized channels. Combiner/equalizers with perfect knowledge of the channels and with channel estimates are considered. As a by-product of the second contribution, we show that Nakahari's MRC combiner [19] (see also Pham [11]) is equivalent to ML combining followed by a zero-forcing FDE.

The simulation results show that for combiners/equalizers with perfect channel knowledge MLD and MRC have the lowest BER while SC+FDE has the highest BER. SC+FDE is about 2 dB worse than the MLD/MRC. MLC+FDE is slightly worse than MLD/MRC and the performance of EGC+FDE is about 1 dB worse than MLD/MRC and 1 dB better than SC+FDE. For the case where channel estimates are used, the same general trends hold. The difference is that at high signal-to-noise ratios, an error floor is observed.

This paper is organized as follows. The post-FFT problem is formulated in Section II. The maximum likelihood solution to the problem is described in Section III. Post-FFT combiners using traditional combining techniques is described in Section IV. Numerical results are presented in Section V followed by conclusions in Section VI. The stochastic channel model used for the computer simulations is described in the Appendix A.

II. PROBLEM FORMULATION

This article focuses on CP-OFDM. Complex-valued baseband equivalent signals and channels [20] are used in the development. A CP-OFDM system is illustrated by the block diagram in Figure 1. At the transmitter, data bits map to N_d symbols drawn from a QAM alphabet $\mathcal{C}$ comprising M constellation points. For channel estimation, N_p pilot symbols drawn from the alphabet $\mathcal{P}$ are inserted. Finally, zeros are inserted to create a sequence of N complex-valued amplitudes that modulate N subcarriers in the frequency domain. (The number of zeros is $N-N_d-N_p$.) Let I_k for $k = 0, \ldots, N-1$ to represent the data symbols, pilot symbols, and zeros, and let $\mathcal{K}_d$ be the set of N_d indexes for data symbols, $\mathcal{K}_p$ be the set of N_p indexes for the pilot symbols, and $\mathcal{K}_z$ be the set $N-N_d-N_p$ indexes for the inserted zeros. The usual practice is to place the zeros at the indexes corresponding to the frequencies farthest from the carrier. Consequently we have

$$\begin{aligned} I_k &\in \mathcal{C}, \quad k \in \mathcal{K}_d \\ I_k &\in \mathcal{P}, \quad k \in \mathcal{K}_p \\ I_k &= 0, \quad k \in \mathcal{K}_z. \end{aligned} \tag{1}$$

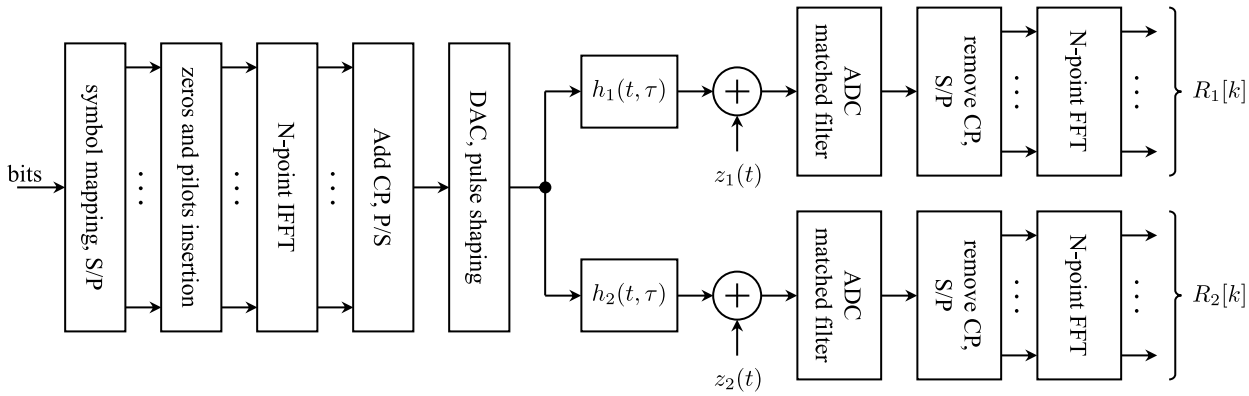

FIGURE 1. OFDM system model with polarization diversity.

I_k amplitude modulates the k-th subcarrier at a discrete-time frequency of $2\pi k/N$. The output of the N-point inverse FFT (IFFT) is

$$d_n = \sum_{k=0}^{N-1} I_k e^{j2\pi kn/N}, \quad 0 \le n < N-1. \tag{2}$$

In the continuous-time domain, an OFDM symbol has a duration of T_s seconds. The subcarrier separation is $\Delta f = 1/T_s$ cycles/s to ensure orthogonality [12]. Adding a cyclic prefix to the sequence d_n produces the sequence s_n. The complex-valued baseband equivalent of the OFDM symbol is

$$s(t) = \sum_n s_n g(t - nT), \tag{3}$$

where $g(t)$ is the pulse shape which is assumed to satisfy the Nyquist no-ISI condition and $T = T_s/N$ s/sample. The cyclic prefix (CP) is inserted to account for the channel delay spread; it makes linear convolution in the continuous-time domain look like circular convolution in the FFT-domain in anticipation of frequency domain equalization.

The complex baseband signal is transmitted from a linearly polarized transmit antenna through a frequency-selective multipath channel. The received signal is characterized by outputs of co-located orthogonally-polarized antenna elements. The time-varying multipath channels that represent the orthogonally-polarized signal components are represented by the time-varying impulse responses $h_1(t,\tau)$ and $h_2(t,\tau)$. After sampling, cyclic prefix removal, and serial-to-parallel conversion, the N-point FFTs of the two signal components are

$$R_1[k] = I_k H_1[k] + Z_1[k], \tag{4}$$
$$R_2[k] = I_k H_2[k] + Z_2[k], \tag{5}$$

for $k = 0, \ldots, N-1$ where $H_1[k]$ and $H_2[k]$ are the FFTs of the sampled channel impulse responses and may be represented samples of the channel frequency responses given by

$$H_m[k] = \begin{cases} H_m(k\Delta f) & 0 \le k \le N/2-1, \\ H_m((k-N)\Delta f) & N/2 \le k \le N-1, \end{cases} \tag{6}$$

for $m = 1, 2$, and $Z_m[k]$ (also for $m = 1, 2$) is the additive thermal noise modeled as a sequence zero-mean circularly symmetric complex-valued normal random variables with autocorrelation function [20]

$$\mathrm{E}\left\{Z_m[k+r]Z_m^*[k]\right\} = 2N_0\delta_r, \tag{7}$$

where N_0 is the power spectral density level (with units W/Hz) of the additive thermal noise, and δ_r is the Kronecker delta. The problem is to produce the "best" estimate of I_k from $R_1[k]$ and $R_2[k]$ for $k = 0, \ldots, N-1$.

III. POST-FFT MAXIMUM LIKELIHOOD DETECTION

Because the noise terms in (4) and (5) are independent, the conditional joint probability density function for $R_1[k]$ and $R_2[k]$ is

$$\begin{aligned} &f(R_1[k], R_2[k]|I_k) \\ &\quad = \frac{1}{2\pi N_0} \exp\left\{-\frac{1}{2N_0}\left|R_1[k] - H_1[k]I_k\right|^2\right\} \\ &\qquad \times \frac{1}{2\pi N_0} \exp\left\{-\frac{1}{2N_0}\left|R_2[k] - H_2[k]I_k\right|^2\right\}. \end{aligned} \tag{8}$$

This conditional probability density function is likelihood function. The log-likelihood function is the natural logarithm of (8) and is given by

$$\begin{aligned} \Lambda(I_k) = &\ln\left(\frac{1}{2\pi N_0}\right) - \left\{\frac{1}{2N_0}\left|R_1[k] - H_1[k]I_k\right|^2\right\} \\ &+ \ln\left(\frac{1}{2\pi N_0}\right) - \left\{\frac{1}{2N_0}\left|R_2[k] - H_2[k]I_k\right|^2\right\}. \end{aligned} \tag{9}$$

Expanding the quadratic terms of (9) and discarding terms and constants which are not functions of I_k produces

$$\begin{aligned} \Lambda(I_k) = &2\mathrm{Re}\left\{I_k^*(H_1^*[k]R_1[k] + H_2^*[k]R_2[k])\right\} \\ &- (H_1^*[k]H_1[k] + H_2^*[k]H_2[k])\,|I_k|^2. \end{aligned} \tag{10}$$

The ML estimate $\hat{I}_k$ is the I_k that maximizes (10):

$$\hat{I}_k = \underset{I_k \in \mathcal{C}}{\mathrm{argmax}}\{\Lambda(I_k)\},\ k \in \mathcal{K}_d. \tag{11}$$

A block diagram of the decision rule (11) is illustrated in Figure 2. Because the noise samples on different subcarriers are uncorrelated, ML detection (MLD) may operate on a subcarrier-by-subcarrier basis. This is in contrast to the case with single-carrier modulations where detection is performed in the time domain; the intersymbol interference generated by frequency selective fading forces the ML detector to be a sequence detector (see [15] or [20, Section 9.3]).

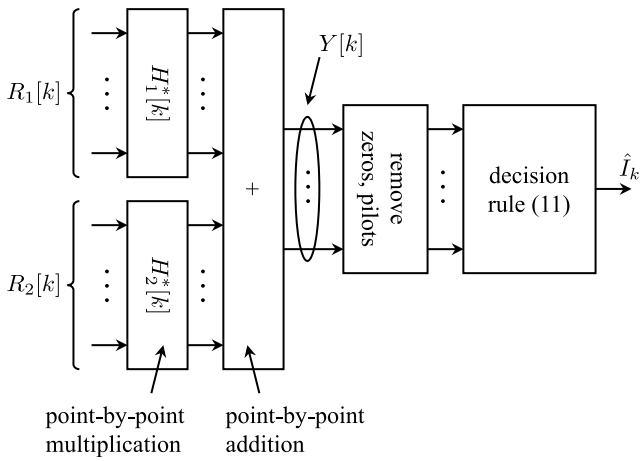

FIGURE 2. A block diagram illustrating ML detection (MLD) operating on $R_1[k]$ and $R_2[k]$ produced in Figure 1.

The MLD detector (11) defines an equivalent discrete-time channel for each subcarrier. Substituting (4) and (5) for $R_1[k]$ and $R_2[k]$, respectively, on the right-hand side of (10) produces

$$Y[k] = H_1^*[k]R_1[k] + H_2^*[k]R_2[k] \tag{12}$$

$$= \left(|H_1[k]|^2 + |H_2[k]|^2\right) I_k + Z[k] \tag{13}$$

where

$$Z[k] = H_1^*[k]Z_1[k] + H_2^*[k]Z_2[k] \tag{14}$$

is a zero-mean circularly symmetric complex-valued normal random variable with variance

$$\mathrm{E}\left\{Z[k]Z^*[k]\right\} = \left(|H_1[k]|^2 + |H_2[k]|^2\right) 2N_0. \tag{15}$$

The interpretation is the k-th symbol I_k passes through a channel defined as

$$H_{\mathrm{eq}}[k] = |H_1[k]|^2 + |H_2[k]|^2 \tag{16}$$

and experiences additive noise whose variance is $2N_0H_{\mathrm{eq}}[k]$. The equivalent channel is illustrated in Figure 3. The ML decision rule (11) is seen to be one that operates on $Y[k]$:

$$\hat{I}_k = \underset{I_k \in \mathcal{C}}{\operatorname{argmax}} \left\{2\mathrm{Re}\left(I_k^* Y[k]\right) - H_{\mathrm{eq}}[k]|I_k|^2\right\}, \quad k \in \mathcal{K}_d. \tag{17}$$

Here, $Y[k]$ is the output of the equivalent channel. The ML estimate of the k-th symbol is the symbol that maximizes the argument in the right-hand side of (17). The ML estimate

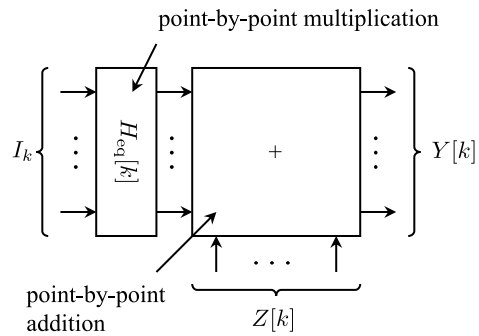

FIGURE 3. The equivalent channel seen by the maximum likelihood detector (17).

maximizes the correlation between $I_k \in \mathcal{C}$ and $Y[k]$ with the removal of $H_{\mathrm{eq}}[k]|I_k|^2$ to account for the case where $I_k \in \mathcal{C}$ have different energies. If all the $I_k \in \mathcal{C}$ had the same energy (e.g., BPSK, QPSK) then the term $H_{\mathrm{eq}}[k]|I_k|^2$ could be omitted.

It is common in the equalization literature (see e.g. [20, Section 9.4] and the references therein) to replace the optimum decision rule (17) by a linear equalizer filter operating on the channel output. Symbol decisions are made on the equalizer filter output using the AWGN decision rule (minimum Euclidean distance rule). In this application, the post-FFT equalizer filter is a frequency-domain equalizer (FDE) filter. The FDE filter is [21]

$$W[k] = \frac{H_{\mathrm{eq}}^*[k]}{|H_{\mathrm{eq}}[k]|^2 + S_Z[k]/\sigma_I^2[k]}, \quad 0 \le k < N-1, \tag{18}$$

where the noise power spectral density $S_Z[k]$ is given by (15) and $\sigma_I^2[k]$ is the variance of I_k.

This approach is illustrated by the general block diagram in Figure 4. Observe that the channel output $Y[k]$ is created by combining, on a subcarrier-by-subcarrier basis, the FFT-domain outputs from the cross-polarized antenna elements. The combining coefficients are, in general, given by $C_1[k]$ and $C_2[k]$. For the present case, $C_1[k] = H_1^*[k]$ and $C_2[k] = H_2^*[k]$. Because the combining follows from the equivalent channel produced by maximum likelihood principles, this combiner is called *maximum likelihood combiner* (MLC) in this article. The combination of MLC and frequency-domain equalization is denoted MLC+FDE.

IV. POST-FFT COMBINING AND EQUALIZATION USING TRADITIONAL COMBINERS

Post-FFT combining combines the received subcarriers on the two channels on a subcarrier-by-subcarrier basis. The combiner output $Y_c[k]$ is

$$Y_c[k] = C_1[k]R_1[k] + C_2[k]R_2[k], \quad k = 0, \ldots, N-1 \tag{19}$$

where $C_1[k]$ and $C_2[k]$ are the combiner coefficients determined by the kind of combining as described below.

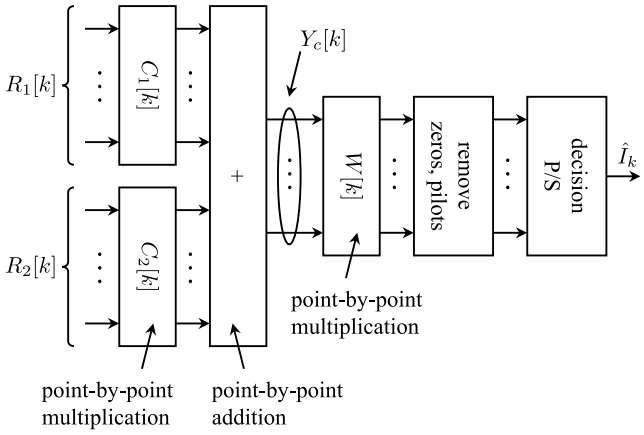

FIGURE 4. Post-FFT combining. The inputs $R_1[k]$ and $R_2[k]$ are produced by the system in Figure 1.

Combining of the form (19) produces an equivalent channel on which the equalizer must operate. Substituting (4) and (5) for $R_1[k]$ and $R_2[k]$, respectively, in (19) produces

$$Y_c[k] = \underbrace{(C_1[k]H_1[k] + C_2[k]H_2[k])}_{H_c[k]} I_k + \underbrace{C_1[k]Z_1[k] + C_2[k]Z_2[k]}_{Z_c[k]}. \quad (20)$$

In this model, $Z_c[k]$ is a zero-mean circularly symmetric complex-valued normal random variable with variance

$$\mathrm{E}\left\{Z_c[k]Z_c^*[k]\right\} = \left(|C_1[k]|^2 + |C_2[k]|^2\right) 2N_0. \quad (21)$$

Nakahari's post-FFT maximum ratio combiner (MRC) [19] (see also Pham [11]) uses the coefficients

$$C_1[k] = \frac{H_1^*[k]}{|H_1[k]|^2 + |H_2[k]|^2} \quad (22)$$

$$C_2[k] = \frac{H_2^*[k]}{|H_1[k]|^2 + |H_2[k]|^2}, \quad (23)$$

for $k = 0, \ldots, N-1$. The equivalent channel is [cf., (20)]

$$H_{\mathrm{MRC}}[k] = 1 \quad (24)$$

and the variance of the additive noise is [cf., (21)]

$$\mathrm{E}\left\{Z_{\mathrm{MRC}}[k]Z_{\mathrm{MRC}}^*[k]\right\} = \frac{2N_0}{|H_1[k]|^2 + |H_2[k]|^2}. \quad (25)$$

In equal gain combining (EGC), the two channels on the k-th subcarrier are co-phased and added. This is accomplished using the coefficients

$$C_1[k] = \frac{1}{2}e^{-j\angle H_1[k]} \quad (26)$$

$$C_2[k] = \frac{1}{2}e^{-j\angle H_2[k]} \quad (27)$$

for $k = 0, \ldots, N-1$. The equivalent channel is [cf., (20)]

$$H_{\mathrm{EGC}}[k] = \frac{1}{2}|H_1[k]| + \frac{1}{2}|H_2[k]| \quad (28)$$

and the variance of the additive noise is [cf., (21)]

$$\mathrm{E}\left\{Z_{\mathrm{EGC}}[k]Z_{\mathrm{EGC}}^*[k]\right\} = N_0. \quad (29)$$

In selection combining (SC), the channel with the highest signal-to-noise ratio is used; the other channel is discarded. Because the noise variance is the same on both channels, the channel with the largest magnitude is the channel with the highest signal-to-noise ratio [8]. The coefficients are

$$C_1[k] = \begin{cases} 1 & |H_1[k]|^2 > |H_2[k]|^2 \\ 0, & \text{otherwise} \end{cases} \quad (30)$$

and $C_2[k]$ is the complement of $C_1[k]$, for $k = 0, \ldots, N-1$. The equivalent channel is [cf., (20)]

$$H_{\mathrm{SC}}[k] = \begin{cases} H_1[k] & |H_1[k]|^2 > |H_2[k]|^2 \\ H_2[k] & \text{otherwise} \end{cases} \quad (31)$$

and the variance of the additive noise is [cf., (21)]

$$\mathrm{E}\left\{Z_{\mathrm{SC}}[k]Z_{\mathrm{SC}}^*[k]\right\} = 2N_0. \quad (32)$$

It is important to note that MRC as defined by the coefficients (22) and (23) performs *both* combing and equalization [see (24)]. Consequently, there is no need for the FDE $W[k]$ in Figure 4 when MRC is used. In contrast, EGC and SC do not perform equalization and require the FDE in Figure 4. The EGC+FDE system uses the EGC coefficients (26) and (27) and the FDE defined by (18) where $H_{\mathrm{eq}}[k]$ is replaced by $H_{\mathrm{EGC}}[k]$. The SC+FDE system uses the SC coefficients (30) and the FDE defined by (18) where $H_{\mathrm{eq}}[k]$ is replaced by $H_{\mathrm{SC}}[k]$.

Further insight into MRC is gained by closer examination. The MRC output $Y_{\mathrm{MRC}}[k]$ is

$$Y_{\mathrm{MRC}}[k] = \frac{H_1^*[k]R_1[k] + H_2^*[k]R_2[k]}{|H_1[k]|^2 + |H_2[k]|^2}, \quad (33)$$

for $k = 0, \ldots, N-1$. Conceptually, the computation of $Y_{\mathrm{MRC}}[k]$ can be performed in two steps. The first step computes the numerator

$$Y_1[k] = H_1^*[k]R_1[k] + H_2^*[k]R_2[k] \quad (34)$$

which, using (4) and (5), may be expressed as

$$Y_1[k] = \left(|H_1[k]|^2 + |H_2[k]|^2\right) I_k + H_1^*[k]Z_1[k] + H_2^*[k]Z_2[k]. \quad (35)$$

This is identical to the channel output in MLD given by (12) and is also the result of maximum likelihood combining. Eq. (35) shows that the equivalent channel is (16).

The second step applies a zero-forcing (ZF) FDE operating on the equivalent channel. The ZF FDE is given by (18) where $S_Z[k] = 0$ for $k = 0, \ldots, N-1$ [20]:

$$W_{\mathrm{ZF}}[k] = \frac{H_{\mathrm{eq}}^*[k]}{|H_{\mathrm{eq}}[k]|^2} = \frac{1}{H_{\mathrm{eq}}[k]}. \quad (36)$$

That is, the ZF equalizer "inverts the channel" and ignores the noise. Applying the equalizer to (34) gives

$$Y_1[k]W_{\mathrm{ZF}}[k] = \left(H_1^*[k]R_1[k] + H_2^*[k]R_2[k]\right) \times \frac{1}{|H_1[k]|^2 + |H_2[k]|^2}. \quad (37)$$

This shows that Nakahari's post-FFT MRC is equivalent to MLC followed by a zero-forcing FDE.

V. COMPARISONS

A. RESULTS I: IDEAL CHANNEL ESTIMATORS

Computer simulations are used to compare the performance of the different combining techniques. The system parameters used for the simulations are summarized in Table 1. Note that in the case of ideal estimators, the pilots are not used for channel estimation (but the pilots are used for channel estimation for the results presented in Section V-B).

TABLE 1. Parameters used for the BER simulations.

Parameter	Value
QAM alphabet	16QAM
Carrier frequency	$f_c = 3.7$ GHz
Subcarrier spacing	$\Delta f = 15$ KHz
Number of data SC	$N_d = 4608$
Number of pilot SC	$N_p = 2048$
FFT length	$N_{FFT} = 8192$

The channels used for the simulations are an ensemble of stochastic channels with polarization state information. The stochastic channel model is described in the Appendix A. The channel is assumed to be fixed during an OFDM symbol, but changes from one OFDM symbol to another.

The stochastic channels are characterized by the power delay profiles and angular spreads illustrated in Figures 5 and 6, respectively. The power delay profile in Figure 5 shows that the channels have unequal power on average. The channel describing vertically-polarized propagation is about 10–15 dB stronger than the channel describing horizontally-polarized propagation. This is to be expected because the transmit antenna is a vertically-polarized element. The power delay profiles also show that these channels are dominated by the line-of-sight propagation path. Because the delays are the same for the vertically- and horizontally-polarized channels, both channels have the same delay spread even though the power delay profiles are different. The difference between the maximum and minimum delays for both channels is 0.15 μs which is consistent with the radii of the reflector spheres surrounding the transmitter and receiver.

The angular spreads are illustrated by the histograms shown in Figure 6. The histogram for the azimuth angle shows that most of the arrivals are caused by reflectors in the hemisphere facing the transmitter. The histogram for the elevation angle shows that most of the arrivals are caused by reflectors above the receiver.

These characteristics, an LOS-dominated channel, a relatively small delay spread, and arrival angles in the direction of the transmitter and above the receiver, are appropriate for a mobile-to-mobile setting.

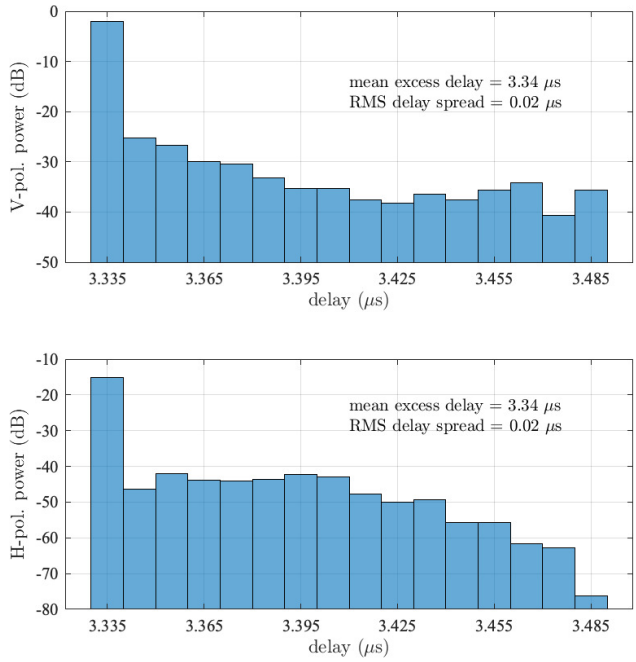

FIGURE 5. Power delay profile for the randomly-generated channels used in the simulations: for the vertically-polarized receive antenna (top); for the horizontally-polarized receive antenna (bottom).

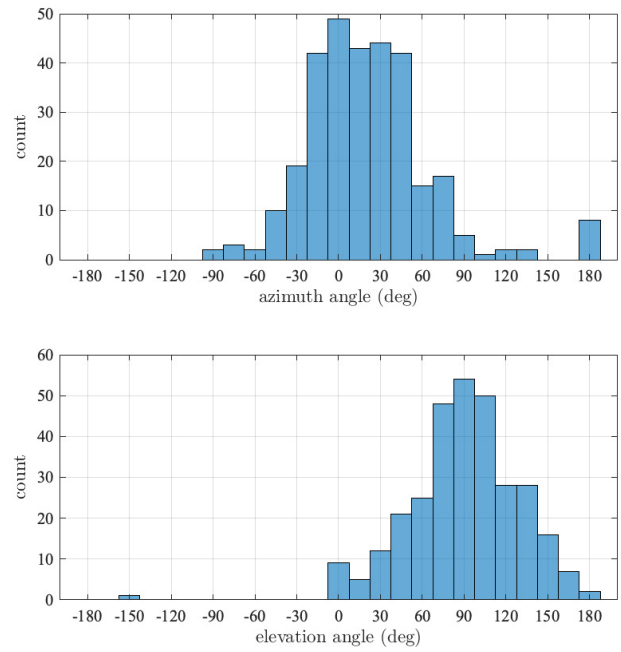

FIGURE 6. Angular spread at the receive antennas for the randomly-generated channels used in the simulations: azimuth angle (top); elevation angle (bottom).

The metric used for the comparisons is the bit error rate (BER). The post-detector BER is used for MLD, the

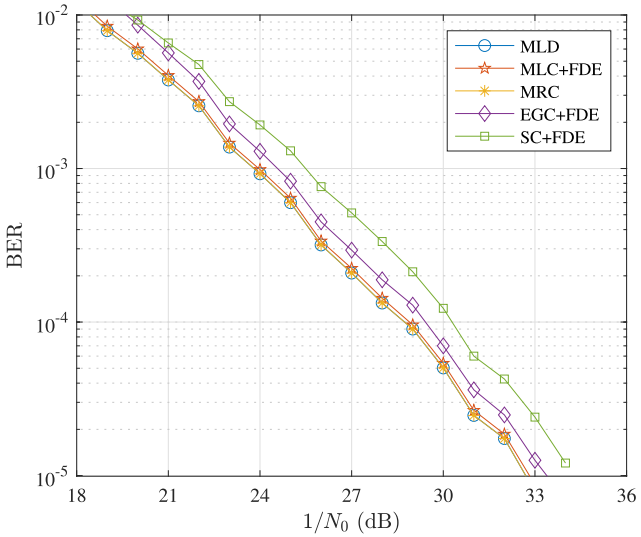

FIGURE 7. Simulated BER performance over the random channels described in the Appendix A for the MLD and four combining techniques assuming an ideal, perfect channel estimate.

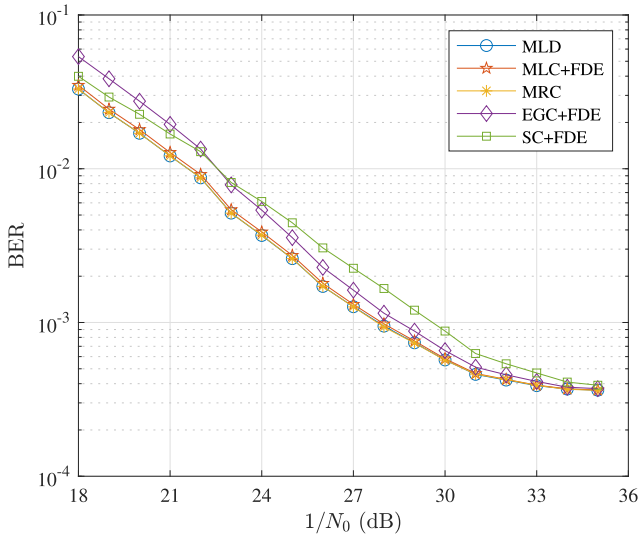

FIGURE 8. Simulated BER performance over the random channels described in the Appendix A for the MLD and four combining techniques using the channel estimates based on $N_p = 2048$ pilot subcarriers.

post-combiner BER for MRC, and the post-equalizer BER for MLC+FDE, EGC+FDE, and SC+FDE.

The results are shown in Figure 7. MLD and MRC are the best and have equivalent BER performance. SC+FDE is the worst, by about 2 dB. The performance of MLC+FDE is very close to that of MLD and MRC. EGC+FDE is about 1 dB inferior to MLD and MRC.

B. RESULTS II: PILOT BASED CHANNEL ESTIMATION

The performance results in the previous section assumed the combiners and equalizers had perfect knowledge of the two channels $H_1[k]$ and $H_2[k]$. In fielded systems, channel estimates replace the true channels and a performance degradation is incurred. The channel estimator used to explore the performance degradation is Weng's least squares (LS) estimator developed in [22]. A brief description of the channel estimator is given in the Appendix B. MLD described in Section III uses $\hat{H}_1[k]$ and $\hat{H}_2[k]$ as explained in Appendix B in place of $H_1[k]$ and $H_2[k]$, respectively. The other detectors are modified as explained in Appendix C.

In the equalized cases, the mismatch between the channel at the equalizer input and the channel used to design the equalizer limits performance. Because the density of the channel estimate is unknown (and correlated with the noise samples), we resort to computer simulations to assess the impact of the use of channel estimates. Computer simulations, based on the parameters listed in Table 1, randomly generated channels as described in the Appendix A, and using the estimator described in Appendix B, are presented in Figure 8. As before, the BER results are the post-detector BER for MLD, the post-combiner BER for MRC, and the post-equalizer BER for MLC+FDE, EGC+FDE, and SC+FDE.

Compared to the ideal estimator results presented Section V-A, the ordering remains the same: MLD and MRC are the best, SC+FDE is the worst. The BER performance of SC+FDE is about 2 dB worse than MLD and MRC for $18 < 1/N_0 < 30$ dB. In the same range, the BER performance of MLC+FDE is very close. What is different here is that the BER performance of all cases exhibits a BER floor at 3.5×10^{-4} for $1/N_0 > 33$ dB. For $1/N_0 > 33$ dB, the BER performance is dominated by channel estimation error instead of thermal noise. Whereas the quality of the channel estimates improves as $1/N_0$ increases, the mismatch between the equalizer and the actual channel remains. This behavior has been observed before in similar systems with equalizers based on channel estimates [23], [24].

VI. CONCLUSION

We developed MLD for post-FFT processing of the dual-polarized antenna outputs with a CP-OFDM waveform in a frequency selective multipath fading environment at 5G FR1 systems. We formulated a detector based on the combining defined by MLD, followed by a FDE, called MLC+FDE. We modeled, simulated, and compared the uncoded BER performance of MLD, MLC+FDE, MRC, EGC+FDE, and SC+FDE applied post FFT and operating over a stochastic channel model with polarization state information. As a byproduct of the analysis, we observed that post-FFT MRC described in [19] and [11] performs both combining and equalization and is equivalent to MLC followed by a zero-forcing FDE.

Computer simulations were performed in two parts. In the first part, the combiner and equalizer (where appropriate) had perfect knowledge of the channels (i.e., ideal channel estimates). The BER results show that MLD and MRC have the same BER and that this BER is the best. The BER

performance of MLC+FDE was a small fraction of a dB worse. The BER performance of EGC+FDE was 1 dB worse than MLD/MRC and that of SC+FDE was 2 dB worse than MLD/MRC.

In the second part, channel estimates, based on pilot subcarriers and interpolation, replaced the true channels. The same trends were observed: the BER performance of MLD and MRC were the best, the post-equalizer BER of MLC+FDE was a close second, EGC+FDE is 1 dB inferior to MLD and MRC, and SC+FDE is 2 dB inferior to MLD and MRC. The difference in this case was presence of a BER floor at low values of N_0 and caused by channel estimation errors.

These results show that the optimum combining and detection strategy produces a 2 dB improvement over the simplest combining strategy (SC). The diversity improvement is limited by the correlation between the two channels that characterize the two polarization states. The BER results show that polarization diversity alone is probably not enough to produce a high-reliability mobile-to-mobile communications link. Some form of error control coding is also required.

APPENDIX A
A STOCHASTIC CHANNEL MODEL WITH POLARIZATION STATE INFORMATION

The channel model used in this article is developed from [16]–[18]. The scenario in this paper considers a 2×1 SIMO scenario illustrated in Figure 9. The channel comprising two time-varying channel impulse responses, one from the vertically-polarized transmit antenna to the vertically polarized receive antenna denoted $h_1(t, \tau)$ and the other from the same vertically-polarized transmit antenna to the horizontally-polarized receive antenna denoted $h_2(t, \tau)$. In this model, the reflectors are on the surface of spheres centered on the transmit and receive antennas. Each impulse response is of the form

$$h_m(t,\tau) = h_m^{(\mathrm{SBT})}(t,\tau) + h_m^{(\mathrm{SBR})}(t,\tau) + h_m^{(\mathrm{DB})}(t,\tau) + h_m^{(\mathrm{LOS})}(t,\tau) \quad (38)$$

for $m = 1, 2$ where $h_m^{(\mathrm{SBT})}(t,\tau)$ is the impulse response of a single-bounce propagation path where the reflector is on the surface of the sphere centered on the transmitter, $h_m^{(\mathrm{SBR})}(t,\tau)$ a single-bounce propagation path where the reflector is on the surface of the sphere centered on the receiver, $h_m^{(\mathrm{DB})}(t,\tau)$ is the impulse response of a double-bounce propagation path where the first reflector is on the surface of the sphere centered on the transmitter and the second reflector is on the surface of the sphere centered on the receiver, and $h_m^{(\mathrm{LOS})}(t,\tau)$ is the impulse response of line-of-sight propagation path between the transmitter and receiver.

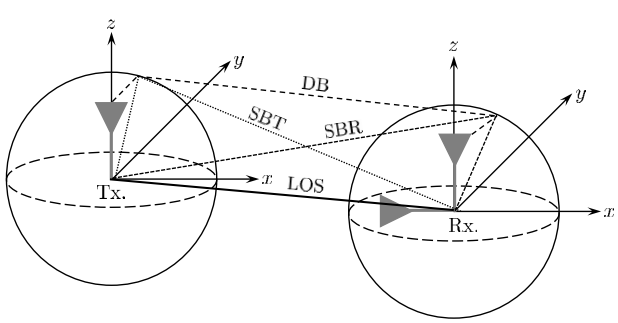

FIGURE 9. Spherical coordinate system for 3D spatially separated 2×1 polarized channel model (reproduced with modifications from [16]–[18]).

Each of the terms in (38) is explained in depth in [16] and [17]. In summary

$$h_1^{(\mathrm{SBT})}(t,\tau) = \sqrt{P_{\mathrm{VV}}}\sqrt{\frac{\eta_{\mathrm{VV}}^{(SBT)}}{K+1}}\frac{1}{\sqrt{M}}\sum_{m=1}^{M}\xi_{\mathrm{VV}}^{(m)}g_{\mathrm{VV}}^{(m)}(t) \times \delta\left(\tau-\tau_{\mathrm{VV}}^{(m)}\right)\mathbf{G}_{\mathrm{T}}^{\dagger}\left(\Omega_{\mathrm{TV}}^{(m)}\right)\Gamma_m\mathbf{G}_{\mathrm{R}}\left(\Omega_{\mathrm{RV}}^{(m)}\right), \quad (39)$$

$$h_1^{(SBR)}(t,\tau) = \sqrt{P_{\mathrm{VV}}}\sqrt{\frac{\eta_{\mathrm{VV}}^{(SBR)}}{K+1}}\frac{1}{\sqrt{N}}\sum_{n=1}^{N}\xi_{\mathrm{VV}}^{(n)}g_{\mathrm{VV}}^{(n)}(t) \times \delta\left(\tau-\tau_{\mathrm{VV}}^{(n)}\right)\mathbf{G}_{\mathrm{T}}^{\dagger}\left(\Omega_{\mathrm{TV}}^{(n)}\right)\Gamma_n\mathbf{G}_{\mathrm{R}}\left(\Omega_{\mathrm{RV}}^{(n)}\right), \quad (40)$$

$$h_1^{(DB)}(t,\tau) = \sqrt{P_{\mathrm{VV}}}\sqrt{\frac{\eta_{\mathrm{VV}}^{(DB)}}{K+1}}\frac{1}{\sqrt{MN}}\sum_{m=1}^{M}\sum_{n=1}^{N}\xi_{\mathrm{VV}}^{(m,n)}g_{\mathrm{VV}}^{(m,n)}(t) \times \delta\left(\tau-\tau_{\mathrm{VV}}^{(m,n)}\right)\mathbf{G}_{\mathrm{T}}^{\dagger}\left(\Omega_{\mathrm{TV}}^{(m)}\right) \times \Gamma_{m,n}\mathbf{G}_{\mathrm{R}}\left(\Omega_{\mathrm{RV}}^{(n)}\right), \quad (41)$$

$$h_1^{(LOS)}(t,\tau) = \sqrt{P_{\mathrm{VV}}}\sqrt{\frac{K}{K+1}}\xi_{\mathrm{VV}}^{(LOS)} \times \delta(\tau-\tau_{\mathrm{VV}}^{(LOS)})\mathbf{G}_{\mathrm{T}}^{\dagger}(\Omega_{TV}^{(LOS)}) \times \Gamma^{(LOS)}\mathbf{G}_{\mathrm{R}}(\Omega_{RV}^{(LOS)}), \quad (42)$$

$$h_2^{(SBT)}(t,\tau) = \sqrt{P_{\mathrm{VH}}}\sqrt{\frac{\eta_{\mathrm{VH}}^{(SBT)}}{K+1}}\frac{1}{\sqrt{M}}\sum_{m=1}^{M}\xi_{\mathrm{VH}}^{(m)}g_{\mathrm{VH}}^{(m)}(t) \times \delta\left(\tau-\tau_{\mathrm{VH}}^{(m)}\right)\mathbf{G}_{\mathrm{T}}^{\dagger}\left(\Omega_{\mathrm{TV}}^{(m)}\right) \times \Gamma_m\mathbf{G}_{\mathrm{R}}\left(\Omega_{\mathrm{RH}}^{(m)}\right), \quad (43)$$

$$h_2^{(SBR)}(t,\tau) = \sqrt{P_{\mathrm{VH}}}\sqrt{\frac{\eta_{\mathrm{VH}}^{(SBR)}}{K+1}}\frac{1}{\sqrt{N}}\sum_{n=1}^{N}\xi_{\mathrm{VH}}^{(n)}g_{\mathrm{VH}}^{(n)}(t) \times \delta\left(\tau-\tau_{\mathrm{VH}}^{(n)}\right)\mathbf{G}_{\mathrm{T}}^{\dagger}\left(\Omega_{\mathrm{TV}}^{(n)}\right) \times \Gamma_n\mathbf{G}_{\mathrm{R}}\left(\Omega_{\mathrm{RH}}^{(n)}\right), \quad (44)$$

$$h_2^{(DB)}(t,\tau) = \sqrt{P_{\mathrm{VH}}}\sqrt{\frac{\eta_{\mathrm{VH}}^{(DB)}}{K+1}}\frac{1}{\sqrt{MN}}\sum_{m=1}^{M}\sum_{n=1}^{N}\xi_{\mathrm{VH}}^{(m,n)}g_{\mathrm{VH}}^{(m,n)}(t) \times \delta\left(\tau-\tau_{\mathrm{VH}}^{(m,n)}\right)\mathbf{G}_{\mathrm{T}}^{\dagger}\left(\Omega_{\mathrm{TV}}^{(m)}\right) \times \Gamma_{m,n}\mathbf{G}_{\mathrm{R}}\left(\Omega_{\mathrm{RH}}^{(n)}\right), \quad (45)$$

TABLE 2. Description of the variables in (39)–(46).

Variable	Description
$P_{\mathrm{VV}}, P_{\mathrm{VH}}$	the average power between the vertically-polarized transmit antenna and the vertically- and horizontally-polarized receive antennas, respectively
K	the Rice factor
$\eta_{\mathrm{VV}}^{(\mathrm{SBT})}, \eta_{\mathrm{VV}}^{(\mathrm{SBR})}, \eta_{\mathrm{VV}}^{(\mathrm{DB})}$	the ratio of power at the vertically-polarized receive antenna to P_{VV} along the SBT, SBR, and DB paths, respectively
$\eta_{\mathrm{VH}}^{(\mathrm{SBT})}, \eta_{\mathrm{VH}}^{(\mathrm{SBR})}, \eta_{\mathrm{VH}}^{(\mathrm{DB})}$	the ratio of power at the horizontally-polarized receive antenna to P_{VH} along the SBT, SBR, and DB paths, respectively
$\xi_{\mathrm{VV}}^{(m)}, \xi_{\mathrm{VH}}^{(m)}$	the amplitude attenuation along the m-th single-bounce path between the transmit antenna and the vertically- and horizontally-polarized receive antennas, respectively; it is a function of of the path loss exponent and the path length
$\xi_{\mathrm{VV}}^{(m,n)}, \xi_{\mathrm{VH}}^{(m,n)}$	the amplitude attenuation along the (m,n)-th double-bounce path between the transmit antenna and the vertically- and horizontally-polarized receive antennas, respectively; it is a function of of the path loss exponent and the path length
$\xi_{\mathrm{VV}}^{(\mathrm{LOS})}, \xi_{\mathrm{VH}}^{(\mathrm{LOS})}$	the amplitude attenuation along the LOS path between the transmit antenna and the vertically- and horizontally-polarized receive antennas, respectively; it is a function of of the path loss exponent and the path length
$g_{\mathrm{VV}}^{(m)}(t), g_{\mathrm{VH}}^{(m)}(t)$	time-varying delay phase terms for the m-th single bounce paths; the phases are functions of the carrier frequency, maximum Doppler frequency, the path delays, the elevation and azimuth angles of departure, the elevation and azimuth angles of arrival, and the direction of travel for the transmitter or receiver (see (7) in [16], [17])
$g_{VV}^{(m,n)}(t), g_{\mathrm{VH}}^{(m,n)}(t)$	the same as $g_{\mathrm{VV}}^{(m)}(t)$ and $g_{\mathrm{VH}}^{(m)}(t)$, respectively, except for the (m,n)-th double bounce path
$\tau_{\mathrm{VV}}^{(m)}, \tau_{\mathrm{VH}}^{(m)}$	the time delay for the m-th single bounce path between the transmit antenna and the vertically- and horizontally-polarized receive antennas, respectively
$\tau_{\mathrm{VV}}^{(m,n)}, \tau_{\mathrm{VH}}^{(m,n)}$	the time delay for the (m,n)-th double bounce path between the transmit antenna and the vertically- and horizontally-polarized receive antennas, respectively
$\tau_{\mathrm{VV}}^{(\mathrm{LOS})}, \tau_{\mathrm{VH}}^{(\mathrm{LOS})}$	the time delay for the LOS path between the transmit antenna and the vertically- and horizontally-polarized receive antennas, respectively
$\mathbf{G}_{\mathrm{T}}(\Omega), \mathbf{G}_{\mathrm{R}}(\Omega)$	the transmit and receive antenna gain matrices, respectively (see (8) in [16], [17]); the entries in $\mathbf{G}_{\mathrm{T}}(\Omega), \mathbf{G}_{\mathrm{R}}(\Omega)$ are functions of the inclination angles of the transmit and receive antennas and the solid angle Ω defined by the the azimuth and elevations angles of the propagation path; the solid angles of interest are $\Omega_{\mathrm{TV}}^{(m)}$, the solid angle of the m-th path leaving the vertically-polarized transmit antenna, $\Omega_{\mathrm{RV}}^{(n)}$, the solid angle of the n-th path arriving the vertically-polarized receive antenna, $\Omega_{\mathrm{RH}}^{(n)}$, the solid angle of the n-th path arriving the horizontally-polarized receive antenna, $\Omega_{\mathrm{TV}}^{(\mathrm{LOS})}$, the solid angle of the LOS path leaving the vertically-polarized transmit antenna, $\Omega_{\mathrm{RV}}^{(\mathrm{LOS})}$, the solid angle of the LOS path arriving the vertically-polarized receive antenna, $\Omega_{\mathrm{RH}}^{(\mathrm{LOS})}$, the solid angle of the LOS path arriving the horizontally-polarized receive antenna
$\mathbf{\Gamma}_m$	2×2 matrices comprising random reflection coefficients; the entries are functions of the random phase shifts between the transmit antenna and the vertically- or horizontally-polarized receive antenna along the m-th single-bounce path, the cross polarization discrimination ratio, and the co-polarization power ratio
$\mathbf{\Gamma}_{m,n}$	the same as $\mathbf{\Gamma}_m$ except for the (m,n)-th double bounce path
$\mathbf{\Gamma}^{(\mathrm{LOS})}$	the same as $\mathbf{\Gamma}_m$ except for the LOS path

$$h_2^{(LOS)}(t,\tau) = \sqrt{P_{\mathrm{VH}}}\sqrt{\frac{K}{K+1}}\xi_{\mathrm{VH}}^{(LOS)} \times \delta\left(\tau - \tau_{\mathrm{VH}}^{(LOS)}\right)\mathbf{G}_{\mathrm{T}}^{\dagger}\left(\Omega_{\mathrm{TV}}^{(LOS)}\right) \times \Gamma^{(LOS)}\mathbf{G}_{\mathrm{R}}\left(\Omega_{\mathrm{RH}}^{(LOS)}\right), \tag{46}$$

where the variables are described in Table 2.

The locations of the scatters on each of the spheres are random. The von Mises distribution was used in [16] and [17] to characterize the azimuth and elevation angles of the scatters relative to their respective sphere centers. The joint von Mises distribution for the azimuth and elevation angles ϕ and θ is parameterized by the means μ_ϕ and μ_θ, the scattering parameters κ_ϕ and κ_θ that control the spread of the angles about their means, and a correlation parameter $\lambda_{\phi\theta}$. We follow [16], [17] and use the von Mises distribution here.

We assume the co-located cross-polarized antenna elements are simple dipoles. The antenna gain for a dipole is found in [25]. We also assume that the antenna gain patterns for vertically and horizontally polarized antenna elements are the power gain patterns of half-wavelength dipole antennas presented in Fig. 5 of [25].

The channel model in [17] also accounts for the polarization coupling effect by including XPD and CPR in the Γ matrices [26]. Absorption due to the user is also captured in this model because absorption due to a user can be observed in

TABLE 3. Parameters of the channel impulse responses in (39)–(46).

Parameter	Symbol and Value
Radius of the spherical volume around the Tx.	$R_{\mathrm{T}} = 10$ m
Radius of the spherical volume around the Rx.	$R_{\mathrm{R}} = 20$ m
Ground distance between Tx. and Rx.	1000 m
Carrier frequency	$f_c = 3.7$ GHz
Maximum doppler frequency associated with Tx.	$f_{\mathrm{T,max}} = 200$ Hz
Maximum doppler frequency associated with Rx.	$f_{\mathrm{R,max}} = 200$ Hz
average transmit power	$P_{\mathrm{VV}} = P_{\mathrm{VH}} = 1$ watt
Rician factor	$K = 4$
Number of scatterers around the Tx.	$M = 8$
Number of scatterers around the Rx.	$N = 33$
Path loss exponent	$\gamma = 2.9$
Power ratio coefficient of SBT	$\eta_{\mathrm{VV}}^{(\mathrm{SBT})} = \eta_{\mathrm{VH}}^{(\mathrm{SBT})} = 1/8$
Power ratio coefficient of SBR	$\eta_{\mathrm{VV}}^{(\mathrm{SBR})} = \eta_{\mathrm{VH}}^{(\mathrm{SBR})} = 1/8$
Power ratio coefficient of DB	$\eta_{\mathrm{VV}}^{(\mathrm{DB})} = \eta_{\mathrm{VH}}^{(\mathrm{DB})} = 3/4$
The direction of azimuth angle where Tx. is moving	$\phi_{\mathrm{vT}} = 0$
The direction of elevation angle where Tx. is moving	$\theta_{\mathrm{vT}} = 0$
The direction of azimuth angle where Rx. is moving	$\phi_{\mathrm{vR}} = \pi/4$
The direction of elevation angle where Rx. is moving	$\theta_{\mathrm{vR}} = \pi/6$
The mean value of the scatterer direction in the azimuth plane	$\mu_\phi = \pi/12$
The mean value of the scatterer direction in the elevation plane	$\mu_\theta = \pi/2$
The parameter to control the spread of scatterers around the mean μ_ϕ for NLOS path	$\kappa_\phi = 3$
The parameter to control the spread of scatterers around the mean μ_θ for NLOS path	$\kappa_\theta = 3$
Inclination angle for the transmitter antenna	0.2443 rad
Inclination angle for the receiver antenna	$\sim \mathcal{U}(0, \pi/2)$
Co-polarization power ratio	CPR = 0 dB
Cross polarization discrimination ratio	$\mathrm{XPD}_{(\mathrm{LOS})} \sim \mathcal{N}(9, 6)$ dB
Cross polarization discrimination ratio	$\mathrm{XPD}_{(\mathrm{NLOS})} \sim \mathcal{N}(8, 6)$ dB

mutual coupling variations [27]. Mutual coupling variations induce changes in polarization coupling. As mentioned in the introduction, the performance of polarization diversity depends on how uncorrelated the outputs of the two antenna elements are. If the effect of the absorption due to the user, and consequently its effect on polarization coupling, increases the correlation of the two antenna outputs, then the performance gain due to polarization diversity combining is reduced, and vice versa.

The parameter values used to generate the random channels are listed in Table 3. The values for the radii of the spheres centered at the transmitter and receiver were selected to model local scatters near the transmitter and receiver. The XPD values were adopted from the 3GPP standard [28]. Because the co-located cross-polarized antenna elements are small, both have the same delays: $\tau_{\mathrm{VV}}^{(m)} = \tau_{VH}^{(m)}$, $\tau_{\mathrm{VV}}^{(m,n)} = \tau_{VH}^{(m,n)}$, and $\tau_{\mathrm{VV}}^{(LOS)} = \tau_{VH}^{(LOS)}$ in (39)–(46).

APPENDIX B
CHANNEL ESTIMATOR

Each OFDM symbol comprises data subcarriers, pilot subcarriers, and zeros. The data subcarrier indexes are in the set $\mathcal{K}_d$ and have unknown amplitudes. The pilot subcarriers, at pilot indexes $\mathcal{K}_p$ have known amplitudes and are positioned in a comb-type arrangement. Channel estimation is performed in two steps

1) Calculate the channel gains at each pilot subcarrier on each channel. The results are $\hat{H}_1[k]$ and $\hat{H}_2[k]$ for $k \in \mathcal{K}_p$.
2) Estimate the channel gains at the data subcarriers using the results from the previous step and interpolation. The results are $\hat{H}_1[k]$ and $\hat{H}_2[k]$ for $k \in \mathcal{K}_d$.

The first step starts with stacking the received pilot subcarriers into $N_p \times 1$ vectors

$$\mathbf{R}_{p,1} = \begin{bmatrix} R_1[k_1] \\ \vdots \\ R_1[k_{N_p}] \end{bmatrix}, \quad \mathbf{R}_{p,2} = \begin{bmatrix} R_2[k_1] \\ \vdots \\ R_2[k_{N_p}] \end{bmatrix} \tag{47}$$

where $k_1, \ldots, k_{N_p}$ are the members of $\mathcal{K}_p$. The vectors of received pilot subcarriers may be expressed as

$$\mathbf{R}_{p,1} = \mathbf{X}_p \mathbf{H}_{p,1} + \mathbf{Z}_{p,1}, \quad \mathbf{R}_{p,2} = \mathbf{X}_p \mathbf{H}_{p,2} + \mathbf{Z}_{p,2} \tag{48}$$

where $\mathbf{X}_p$ is an $N_p \times N_p$ diagonal matrix with the N_p pilot amplitudes on its main diagonal and $\mathbf{H}_{p,1}$, $\mathbf{H}_{p,2}$, $\mathbf{Z}_{p,1}$, and

$\mathbf{Z}_{p,2}$ are formed from $H_1[k]$, $H_2[k]$, $Z_1[k]$ and $Z_2[k]$, respectively, in the same way $\mathbf{R}_{p,1}$ and $\mathbf{R}_{p,2}$ were formed from $R_1[k]$ and $R_2[k]$, respectively. The LS estimates for the pilot subcarrier channel gains are

$$\hat{\mathbf{H}}_{p,1} = \mathbf{X}_p^{-1}\mathbf{R}_{p,1}, \quad \hat{\mathbf{H}}_{p,2} = \mathbf{X}_p^{-1}\mathbf{R}_{p,2}. \tag{49}$$

The second step uses DFT-based interpolation to compute the channel gains at the data subcarriers. This is accomplished by first computing the N_p-point inverse DFT of the pilot subcarrier channel gains:

$$\mathbf{g}_{s,1} = \text{IDFT}(\hat{\mathbf{H}}_{p,1}), \quad \mathbf{g}_{s,2} = \text{IDFT}(\hat{\mathbf{H}}_{p,2}). \tag{50}$$

Next, $\mathbf{g}_{s,1}$ and $\mathbf{g}_{s,2}$ are zero-padded ($N - N_p$ zeros are appended to the end) to produce

$$\mathbf{g}_1 = \begin{bmatrix} \mathbf{g}_{s,1} \\ \mathbf{0}_{(N-N_p)\times 1} \end{bmatrix}, \quad \mathbf{g}_2 = \begin{bmatrix} \mathbf{g}_{s,2} \\ \mathbf{0}_{(N-N_p)\times 1} \end{bmatrix} \tag{51}$$

where $\mathbf{0}_{(N-N_p)\times 1}$ is the $(N - N_p) \times 1$ vector of zeros. Finally, the channel gains at *all* subcarriers are given by the length-N DFT of $\mathbf{g}_1$ and $\mathbf{g}_2$:

$$\hat{\mathbf{H}}_1 = \text{DFT}(\mathbf{g}_1), \quad \hat{\mathbf{H}}_2 = \text{DFT}(\mathbf{g}_2) \tag{52}$$

where

$$\hat{\mathbf{H}}_1 = \begin{bmatrix} \hat{H}_1[0] \\ \vdots \\ \hat{H}_1[N-1] \end{bmatrix}, \quad \hat{\mathbf{H}}_2 = \begin{bmatrix} \hat{H}_2[0] \\ \vdots \\ \hat{H}_2[N-1] \end{bmatrix}. \tag{53}$$

The zero-padded DFT is used to perform interpolation. The computational efficiency of the FFT (to compute the DFT) makes this a computationally efficient channel estimator.

APPENDIX C
DETECTORS WITH THE ESTIMATED CHANNELS

MLC+FDE: The equalizer in MLC+FDE operates on the combiner output

$$Y_{MLC}^{(\text{est})}[k] = \hat{H}_1^*[k]R_1[k] + \hat{H}_2^*[k]R_2[k] \tag{54}$$

for $k = 0, \ldots, N-1$. Using (4) and (5), $Y_{MLC}^{(\text{est})}[k]$ may be expressed as

$$\begin{aligned} Y_{MLC}^{(\text{est})}[k] = &\left(\hat{H}_1^*[k]H_1[k] + \hat{H}_2^*[k]H_2[k]\right) I_k \\ &+ \hat{H}_1^*[k]Z_1[k] + \hat{H}_2^*[k]Z_2[k]. \end{aligned} \tag{55}$$

The equalizer operates on the equivalent channel

$$H_{MLC}^{(\text{est})}[k] = \hat{H}_1^*[k]H_1[k] + \hat{H}_2^*[k]H_2[k] \tag{56}$$

but is *designed* to operate on the channel

$$H_{MLC}^{(\text{eq})}[k] = |\hat{H}_1[k]|^2 + |\hat{H}_2[k]|^2. \tag{57}$$

MRC: The MRC detector operates on the combiner output

$$Y_{\text{MRC}}^{(\text{est})}[k] = \frac{\hat{H}_1^*[k]R_1[k]}{|\hat{H}_1[k]|^2 + |\hat{H}_2[k]|^2} + \frac{\hat{H}_2^*[k]R_2[k]}{|\hat{H}_1[k]|^2 + |\hat{H}_2[k]|^2} \tag{58}$$

for $k = 0, \ldots, N-1$. Using (4) and (5), $Y_{\text{MRC}}^{(\text{est})}[k]$ may be expressed as

$$\begin{aligned} Y_{\text{MRC}}^{(\text{est})}[k] = &\frac{\hat{H}_1^*[k]H_1[k] + \hat{H}_2^*[k]H_2[k]}{|\hat{H}_1[k]|^2 + |\hat{H}_2[k]|^2} I_k \\ &+ \frac{\hat{H}_1^*[k]Z_1[k] + \hat{H}_2^*[k]Z_2[k]}{|\hat{H}_1[k]|^2 + |\hat{H}_2[k]|^2}. \end{aligned} \tag{59}$$

The detector assumes

$$\frac{\hat{H}_1^*[k]H_1[k] + \hat{H}_2^*[k]H_2[k]}{|\hat{H}_1[k]|^2 + |\hat{H}_2[k]|^2} \approx 1. \tag{60}$$

EGC+FDE: The equalizer in EGC+FDE operates on the combiner output

$$Y_{EGC}^{(\text{est})}[k] = \frac{1}{2}e^{-j\angle\hat{H}_1[k]}R_1[k] + \frac{1}{2}e^{-j\angle\hat{H}_2[k]}R_2[k] \tag{61}$$

for $k = 0, \ldots, N-1$. Using (4) and (5), $Y_{EGC}^{(\text{est})}[k]$ may be expressed as

$$\begin{aligned} Y_{\text{EGC}}^{(\text{est})}[k] = &\left(\frac{1}{2}|H_1[k]|e^{j\left(\angle H_1[k] - \angle\hat{H}_1[k]\right)}\right. \\ &\left. + \frac{1}{2}|H_2[k]|e^{j\left(\angle H_2[k] - \angle\hat{H}_2[k]\right)}\right) I_k \\ &+ \frac{1}{2}e^{-j\angle\hat{H}_1[k]}Z_1[k] + \frac{1}{2}e^{-j\angle\hat{H}_2[k]}Z_2[k]. \end{aligned} \tag{62}$$

The equalizer operates on the equivalent channel

$$\begin{aligned} H_{\text{EGC}}^{(\text{est})}[k] = &\frac{1}{2}|H_1[k]|e^{j\left(\angle H_1[k] - \angle\hat{H}_1[k]\right)} \\ &+ \frac{1}{2}|H_2[k]|e^{j\left(\angle H_2[k] - \angle\hat{H}_2[k]\right)} \end{aligned} \tag{63}$$

but is *designed* to operate on the channel

$$H_{\text{EGC}}^{(\text{eq})}[k] = \frac{1}{2}|\hat{H}_1[k]| + \frac{1}{2}|\hat{H}_2[k]|. \tag{64}$$

SC+FDE: The equalizer in SC+FDE operates on the combiner output

$$Y_{\text{SC}}^{(\text{est})}[k] = \hat{C}_1[k]R_1[k] + \hat{C}_2[k]R_2[k] \tag{65}$$

where

$$\hat{C}_1[k] = \begin{cases} 1 & |\hat{H}_1[k]|^2 > |\hat{H}_2[k]|^2 \\ 0 & \text{otherwise} \end{cases} \tag{66}$$

and $\hat{C}_2[k]$ is the complement of $\hat{C}_1[k]$ for $k = 0, \ldots, N-1$. The equalizer operates on the equivalent channel

$$H_{\text{SC}}^{(\text{est})}[k] = \begin{cases} H_1[k] & |\hat{H}_1[k]|^2 > |\hat{H}_2[k]|^2 \\ H_2[k] & \text{otherwise} \end{cases} \tag{67}$$

but is *designed* to operate on the channel

$$H_{\text{SC}}^{(\text{eq})}[k] = \begin{cases} \hat{H}_1[k] & |\hat{H}_1[k]|^2 > |\hat{H}_2[k]|^2 \\ \hat{H}_2[k] & \text{otherwise.} \end{cases} \tag{68}$$

REFERENCES

[1] M.-Y. Li, Z.-Q. Xu, Y.-L. Ban, Q.-L. Yang, and Q.-Q. Zhou, "Eight-port dual-polarized MIMO antenna for 5G smartphone applications," in *Proc. IEEE 5th Asia–Pacific Conf. Antennas Propag. (APCAP)*, Jul. 2016, pp. 195–196.

[2] F. Arabian, G. P. Nordin, and M. Rice, "On the Ungerboeck and Forney observation models for spatial combining and their application to 5G millimeter-wave bands," *IEEE Access*, vol. 9, pp. 22214–22231, 2021.

[3] W. C. Y. Lee and Y. Yeh, "Polarization diversity system for mobile radio," *IEEE Trans. Commun.*, vol. COM-20, no. 5, pp. 912–923, Oct. 1972.

[4] R. G. Vaughan, "Polarization diversity in mobile communications," *IEEE Trans. Veh. Technol.*, vol. 39, no. 3, pp. 177–186, Aug. 1990.

[5] D. Lee, G. J. Saulnier, Z. Ye, and M. J. Medley, "Antenna diversity for an OFDM system in a fading channel," in *Proc. IEEE Mil. Commun. (MILCOM)*, vol. 2, Nov. 1999, pp. 1104–1109.

[6] S. B. Slimane, "A low complexity antenna diversity receiver for OFDM based systems," in *Proc. IEEE Int. Conf. Commun., Conf. Rec. (ICC)*, Helsinki, Finland, Jun. 2001, pp. 1147–1151.

[7] H. Matsuoka and H. Shoki, "Comparison of pre-FFT and post-FFT processing adaptive arrays for OFDM systems in the presence of co-channel interference," in *Proc. 14th IEEE Proc. Pers., Indoor Mobile Radio Commun. (PIMRC)*, vol. 2, Sep. 2003, pp. 1603–1607.

[8] M. I. Rahman, S. S. Das, F. H. P. Fitzek, and R. Prasad, "Pre- and post-DFT combining space diversity receiver for wideband multi-carrier systems," in *Proc. 8th Conf. Wireless Pers. Multimedia Commun.*, Aalborg, Denmark, 2005, pp. 1–5.

[9] A. Dammann and S. Kaiser, "Standard conformable antenna diversity techniques for OFDM and its application to the DVB-T system," in *Proc. IEEE Global Telecommun. Conf. (GLOBECOM)*, San Antonio, TX, USA, Nov. 2001, pp. 3100–3105.

[10] X. Ouyang, M. Ghosh, and J. P. Meehan, "Optimal antenna diversity combining for IEEE 802.11 a system," *IEEE Trans. Consum. Electron.*, vol. 48, no. 3, pp. 738–742, Aug. 2002.

[11] D. Pham, J. Gao, T. Tabata, H. Asato, S. Hori, and T. Wada, "Implementation of joint pre-FFT adaptive array antenna and post-FFT space diversity combining for mobile ISDB-T receiver," *IEICE Trans. Commun.*, vol. 91, no. 1, pp. 127–138, Jan. 2008.

[12] F. Arabian, M. Rice, and R. Q. Hu, "Who's on first in 5G mobile networks: Equalizers or polarization diversity combiners?" in *Proc. Intermountain Eng., Technol. Comput. (IETC)*, Oct. 2020, pp. 1–6.

[13] S. Mumtaz, K. M. S. Huq, and J. Rodriguez, "Direct mobile-to-mobile communication: Paradigm for 5G," *IEEE Wireless Commun.*, vol. 21, no. 5, pp. 14–23, Oct. 2014.

[14] Z. Li, F. S. Moya, F. Gabor, J. M. B. Da Silva, Jr., K. Koufos, M. Dohler, and T. Nakamura, *Device-to-Device (D2D) Communications*. Cambridge, U.K.: Cambridge Univ. Press, 2016, pp. 107–136.

[15] K. Scott, E. B. Olasz, and A. Sendyk, "Diversity combining with MLSE equalisation," *IEE Proc. Commun.*, vol. 145, no. 2, pp. 105–108, 1998.

[16] J. Chen and T. Pratt, "Diversity measure of co-polarized and polarized MIMO architectures over wideband mobile-to-mobile channels," in *Proc. IEEE Mil. Commun. Conf.*, San Diego, CA, USA, Nov. 2013, pp. 1262–1267.

[17] J. Chen and T. G. Pratt, "Three-dimensional geometry-based stochastic modeling and performance of 4×4 space-polarization mobile-to-mobile wideband MIMO channels," in *Proc. IEEE Global Commun. Conf. (GLOBECOM)*, Dec. 2013, pp. 3936–3941.

[18] Y. Yuan, C.-X. Wang, X. Cheng, B. Ai, and D. I. Laurenson, "Novel 3D geometry-based stochastic models for non-isotropic MIMO vehicle-to-vehicle channels," *IEEE Trans. Wireless Commun.*, vol. 13, no. 1, pp. 298–309, Jan. 2014.

[19] S. Nakahara, H. Hamazumi, K. Shibuya, and M. Sasaki, "An application of diversity combining techniques to broadcasting wave relay station for ISDB-T," *ITE Tech. Rep.*, vol. 25, pp. 7–12, Mar. 2001.

[20] J. Proakis and M. Salehi, *Digital Communications*, 5th ed. New York, NY, USA: McGraw-Hill, 2007.

[21] H. Sari, G. Karam, and I. Jeanclaud, "Frequency-domain equalization of mobile radio and terrestrial broadcast channels," in *Proc. IEEE Commun., Global Bridge (GLOBECOM)*, vol. 1, Nov./Dec. 1994, pp. 1–5.

[22] F. Weng, C. Yin, and T. Luo, "Channel estimation for the downlink of 3GPP-LTE systems," in *Proc. 2nd IEEE Int. Conf. Netw. Infrastruct. Digit. Content*, Sep. 2010, pp. 1042–1046.

[23] D. Van Welden, F. Simoens, H. Steendam, and M. Moeneclaey, "Impact of channel estimation error on the performance of linear FIR equalizers for frequency selective MIMO channels," in *Proc. Benelux Symp. Commun. Veh. Technol.*, 2005, pp. 1–6.

[24] C.-T. Lam and D. D. Falconer, "Effects of channel estimation errors on BER performance of DFT-precoded OFDM systems," in *Proc. 9th Int. Wireless Commun. Mobile Comput. Conf. (IWCMC)*, Jul. 2013, pp. 900–905.

[25] T. Taga, "Analysis for mean effective gain of mobile antennas in land mobile radio environments," *IEEE Trans. Veh. Technol.*, vol. 39, no. 2, pp. 117–131, May 1990.

[26] C. Oestges, B. Clerckx, M. Guillaud, and M. Debbah, "Dual-polarized wireless communications: From propagation models to system performance evaluation," *IEEE Trans. Wireless Commun.*, vol. 7, no. 10, pp. 4019–4031, Oct. 2008.

[27] A. A. H. Azremi, J. Ilvonen, C.-H. Li, J. Holopainen, and P. Vainikainen, "Influence of the user's hand on mutual coupling of dual-antenna structures on mobile terminal," in *Proc. 6th Eur. Conf. Antennas Propag. (EUCAP)*, Mar. 2012, pp. 1222–1226.

[28] *5G; Study on Channel Model for Frequencies From 0.5 to 100 GHz*, ESTI, 3GPP, document 38.901, 2017.

FARAH ARABIAN (Graduate Student Member, IEEE) received the B.Sc. degree in electrical engineering from Sadjad University of Technology, Mashhad, Iran, in 2010, the M.Sc. degree in communications engineering from Amirkabir University of Technology, Tehran, Iran, in 2013, and the Ph.D. degree in electrical and computer engineering from Brigham Young University, Provo, UT, USA in 2022.

She is currently working as a Cellular Engineer with Apple Inc., Cupertino, CA, USA. She worked at Huawei and Nokia, as an UMTS/LTE RF Planning and Optimization Engineer, from 2014 to 2016 and 2016 to 2017, respectively. Her research interests include 5G cellular networks, digital communication theory, and signal processing.

MICHAEL RICE (Fellow, IEEE) received the Ph.D. degree from Georgia Tech, Atlanta, GA, USA, in 1991.

He was with Digital Transmission Systems, Inc., Atlanta, and joined the faculty with Brigham Young University, Provo, UT, USA, in 1991, where he is currently a Professor with the Department of Electrical and Computer Engineering. From 1994 to 1995, he was a NASA/ASEE Summer Faculty Fellow with the Jet Propulsion Laboratory, Pasadena, CA, USA, where he worked on land mobile satellite systems. From 1999 to 2000, he was a Visiting Scholar with the Communication Systems and Signal Processing Institute, San Diego State University. His research interests include digital communication theory and statistical signal processing with a special emphasis on applications to aeronautical telemetry and software radio design. He has been a consultant to both government and industry on telemetry related issues and currently serves as an Associate Member of the Telemetry Group of the Range Commander's Council. He is a member of the IEEE Communications Society and is the Past Chair of the Communication Theory Technical Committee. He is a past member of the Board of Governors for the Aerospace and Electronic Systems Society. He is also a member of the Aerospace and Electronic Systems Society and is the Editor-in-Chief of IEEE Transactions on Aerospace and Electronic Systems.